Ellipticity effects and the contributions of long orbits in nonsequential double ionization of atoms

N. I. Shvetsov-Shilovski,[1] S. P. Goreslavski,[1] S. V. Popruzhenko,[1,2] and W. Becker[3]
[1]*Moscow State Engineering Physics Institute, Kashirskoe Shosse 31, 115409, Moscow, Russia*
[2]*Max-Planck-Institut für Kernphysik, Postfach 103980, 69029 Heidelberg, Germany*
[3]*Max-Born-Institut, Max-Born-Strasse 2a, 12489 Berlin, Germany*
(Received 21 January 2008; published 5 June 2008)

Using a semiclassical model based on tunneling, electron kinematics in the laser field, and phase space volume, we evaluate the ion and electron momentum distributions in nonsequential double ionization of a model atom by an elliptically polarized laser field. For ellipticities exceeding approximately 0.3, we find that the shortest quantum orbit (having the shortest travel time) no longer dominates the double-ionization rate, in contrast to the case of linear polarization. Simultaneously we observe significant violations of symmetry patterns in the ion-momentum distributions and the electron-electron momentum correlations, compared with the case of linear polarization. These violations are very sensitive to the laser pulse duration because of the absence of the late returns for very short pulses. Some of these qualitative effects in the photoelectron distributions should be experimentally detectable. Observation would verify the significance of the late returns and the underlying quantum-orbit concept.

DOI: 10.1103/PhysRevA.77.063405 PACS number(s): 32.80.Rm, 32.80.Wr

I. INTRODUCTION

Theoretical model-based treatments of strong-field ionization and related laser-induced phenomena almost always rely on the strong-field approximation (SFA). The latter admits a very transparent interpretation with high predictive power in terms of "quantum orbits," which has afforded many insights into the physics of above-threshold ionization (ATI), high-order harmonic generation (HHG), nonsequential double and multiple ionization (NSDI), and the rapidly expanding field of attosecond physics. According to this concept, the ionization amplitude can be written as a coherent superposition of the contributions of quantum orbits [1,2]. These are built on classical electron orbits in the presence of the laser field that, loosely speaking, start at some time from the position of the ion and return back to it at a later time. At these returns, an additional interaction between the electron and the ion may occur, which may result in elastic scattering, recombination, or impact ionization of other electrons (see Refs. [3,4] for reviews).

The classical trajectory of the ionized electron driven by a linearly polarized laser field may return to its parent ion arbitrarily often, but in most cases only the first return—the one that corresponds to the shortest travel time in the continuum—provides the dominant contribution to the amplitude. The subsequent returns corresponding to longer travel times are less important because of quantum-mechanical wave packet spreading. This has made it difficult to identify the effects of such long orbits in the experimental data because they are usually hidden under the dominating signal from the shortest orbits. Observation of such effects would provide, however, a direct justification of the quantum orbit concept.

Up to now, several significant achievements have been made in this direction. It was shown that near the closing of ionization channels, when with increasing laser intensity the ponderomotively upshifted ionization potential becomes equal to the energy of an integer number of laser photons, the contributions of a large number of long orbits to the ionization amplitude may add up coherently. This causes very pronounced enhancements in the high-energy part of the ATI spectrum, which by now have been widely studied in theory and well documented experimentally (see Ref. [5], and references therein). A similar effect was predicted for HHG [6] and NSDI [7] but the experimental confirmation was less clear for HHG [6] and the effect has never been seen for NSDI. These enhancements are expected to be most pronounced for a field with linear polarization.

Compared with the case of linear polarization, the kinematics caused by an elliptically polarized field are genuinely two dimensional. This reveals features of the strong-field ionization dynamics that are not accessible with a linearly polarized laser field. The effects of classical dodging [8–10] and Coulomb-induced symmetry violation [11–13] experimentally observed in *direct* ATI spectra could be mentioned as examples. More subtle effects occur in *high-order* ATI and HHG due to the distortion of quantum orbits by the elliptically polarized field. This manifests itself, for example, in ellipticity-dependent interference patterns and a staircase structure of the spectrum [2,12,14]. The advantage of elliptical polarization for the verification of the significance of the late returns can be understood with the help of simple semiclassical arguments: In a linearly polarized field, the electron starts with zero velocity, corresponding to the situation of tunneling. For elliptical polarization, in order that the electron return to the position of the ion it has to depart with nonzero velocity. While this allows the electron to return, it exacts a high price: the classical action assigns a much reduced weight to the contribution of such an orbit. This has the simple consequence that high-order ATI and NSDI rates decrease quickly with increasing ellipticity. There are, however, further consequences. Different orbits acquire different initial velocities, and the shortest orbits, which dominate the rates for linear polarization and have the highest cutoff energy, require the highest initial velocities in order that they return. Hence, longer orbits may have higher weights in the superposition. This is the origin of the aforementioned stair-

case structure of the high-order ATI spectrum for an elliptically polarized field [14].

In the context of the SFA at fixed intensity, the staircase structure is a qualitative effect whose observation would lend strong support to the underlying picture of quantum orbits. However, in experiments the combined effect of focal averaging and intensity-dependent enhancements [5] can generate similar-looking structures. Therefore, it is highly desirable to have a different *qualitative* effect whose observation would support the physical significance of long quantum orbits. In this paper, we will identify and discuss such an effect in NSDI by an elliptically polarized laser field. We will consider the momentum correlation of the two electrons released in NSDI as well as the momentum distribution of the doubly charged ion. We shall show that the contributions of the long orbits in NSDI by a field with significant elliptical polarization qualitatively modify the momentum distributions that result from just the two shortest orbits. The latter distributions can still be seen in experiments, but this requires a pulse short enough to render the longer orbits obsolete. Few-cycle pulses as they have been employed in recent experiments would serve this purpose. The upshot is a very pronounced difference in the momentum distributions caused by long and by short orbits whose observation would strongly confirm the underlying theory.

As mentioned above, in this paper we will be concerned with "nonsequential double ionization." This term refers to the case when two electrons are ejected in one coherent process, so that the rate is not the product of two single-ionization rates. It was first proposed in Refs. [15,16] that a nonsequential channel must contribute to double ionization. NSDI requires electron-electron (e-e) correlation as a precondition for its very existence. The actual mechanism of this correlation was debated for many years. By now, there is consensus that—for rare gases irradiated by an intense near-infrared laser—NSDI is caused by the recollision mechanism [17], the same that is also responsible for HHG and high-order ATI. However, the details significantly depend on the atomic species. For reviews, see Ref. [18].

Thus far, only initial steps have been taken toward an *ab initio* calculation of ion- and electron-momentum distributions of NSDI at infrared laser frequencies, namely, for few-cycle pulses and for the simplest case of helium with reduced dimensionality [19]. Other fully quantum-mechanical calculations are in the context of *S*-matrix theory and build on the Feynman diagram that incorporates rescattering [20,21]. Besides, classical-trajectory simulations, which start from quantum-mechanical tunneling [22] or from classical ensembles [23], have also afforded important insights into NSDI.

All these theoretical achievements, however, have been restricted to the case of linear polarization. Their generalization to an elliptically polarized field is extremely demanding if not impossible because of the computational effort required. Experimentally, several papers have presented measurements of the yield of doubly charged ions produced by circular polarization [26–29]. For an elliptically polarized field, NSDI was only observed for magnesium in Ref. [28], but under conditions (low intensity, so that the maximum energy of the returning photoelectron is far below the second ionization potential) where it cannot be attributed to the rescattering mechanism. Otherwise, we are unaware of theoretical or experimental work concerned with elliptical polarization.

Here we present a very simple model of NSDI in an elliptically polarized field, within which all required calculations are doable. The model is based on the fact that, except for the initial tunneling, NSDI is a largely classical process, provided the energy of the recolliding electron is significantly larger than the ionization energy of the second (bound) electron. If this is the case, then a simplified version of the *S*-matrix element, which contains the quasistatic tunneling rate, but is classical otherwise, has been shown to yield results virtually identical with the fully quantum-mechanical results [24,25]. We modify this approach by incorporating the ellipticity and apply it to calculate the momentum distributions of the doubly charged ions and the associated e-e longitudinal-momentum distributions, whose analysis has provided much insight for linear polarization.

II. CLASSICAL MODEL

Within the aforementioned classical model [24,25] the differential probability of NSDI with emission of electrons with drift momenta $\mathbf{p}_1$ and $\mathbf{p}_2$ is given by

$$\frac{dN}{d^3\mathbf{p}_1 d^3\mathbf{p}_2} \equiv w(\mathbf{p}_1,\mathbf{p}_2) \sim \int dt \frac{R(t)}{(t'-t)^3} |V_{\mathbf{p}_1\mathbf{p}_2}|^2 \delta\Big(E(t') - I_2 - \frac{1}{2}[\mathbf{p}_1 - \mathbf{A}(t')]^2 - \frac{1}{2}[\mathbf{p}_2 - \mathbf{A}(t')]^2\Big). \quad (1)$$

Here $R(t)$ is the time-dependent ionization rate for the first electron, which tunnels out of the atom at the time t and returns to the position of the parent ion at the time t', which is a function of t, with the kinetic energy $E(t')$. Upon its return, it dislodges the second bound electron (whose ionization potential is I_2) in an inelastic collision for which the δ function expresses energy conservation. The integration variable t enters the argument of the δ function via the function $E(t')$, where $t' \equiv t'(t)$ [see Eq. (16) below]. The factor $(t'-t)^{-3}$ accounts for quantum-mechanical spreading of the ionized wave packet while it is traveling. The model (1) disregards interference effects both in the processes of tunneling and of recollision.

We assume for the e-e interaction a three-body contact interaction located at the position of the ion. In this case, the form factor $V_{\mathbf{p}_1\mathbf{p}_2}$, which reflects the cross section of the inelastic process, is a constant and we drop it from Eq. (1). Such a contact interaction has reproduced the data for neon quite well while, surprisingly, the Coulomb interaction yields results in disagreement with the data [30]. Of course, this is not to say that the e-e interaction is not Coulombic, but rather that the respective diagram disregards important features, which can be partly healed by taking a three-body contact (effective) interaction. Recent experimental data for helium, recorded with higher resolution than before, do show some features associated with the Coulomb interaction [31], so that an optimal choice of the interaction matrix element in Eq. (1) remains an open question. Our results are expected to

be more relevant for neon where calculations with the contact interaction and linear polarization have shown the best agreement with the data. The vector potential $\mathbf{A}(t)=(F_0/[\omega\sqrt{1+\xi^2}])(\cos\omega t,-\xi\sin\omega t,0)$ of the field with ellipticity ξ is related to the electric force acting on an electron by $\mathbf{F}(t)=-d\mathbf{A}(t)/dt$. The electron's kinetic energy is $\varepsilon_{\mathbf{k}}(t)=[\mathbf{k}-\mathbf{A}(t)]^2/2$, with $\mathbf{k}$ its drift momentum. We use atomic units, i.e., $e=m=\hbar=1$, and the ponderomotive energy is $U_P=F_0^2/(4\omega^2)\equiv P_F^2/4$ regardless of the ellipticity ξ.

A. Tunneling rate

In Eq. (1), the rate $R(t)$ is defined as [13]

$$R(t)\propto\frac{F_a^2}{F^3(t)}\frac{\sqrt{\ddot{\varepsilon}_{\mathbf{k}}(t)}}{\sqrt{1+\varepsilon_{\mathbf{k}}(t)/I_1}}\exp\left\{-\frac{2F_a}{3\sqrt{\ddot{\varepsilon}_{\mathbf{k}}(t)}}\left[1+\frac{\varepsilon_{\mathbf{k}}(t)}{I_1}\right]^{3/2}\right\},\tag{2}$$

where $F_a=(2I_1)^{3/2}$ is the characteristic atomic field for the first electron whose ionization potential is I_1. This rate is obtained from the standard SFA ionization amplitude [32,33] calculated by the saddle-point method

$$M(\mathbf{k})\sim\frac{1}{\sqrt{\ddot{S}(\mathbf{k},t_s)}}\exp[iS(\mathbf{k},t_s)].\tag{3}$$

Here

$$S(\mathbf{k},t)=\int^t d\tilde{t}\,[\varepsilon_{\mathbf{k}}(\tilde{t})+I_1]$$

is the classical action for an electron with the drift momentum $\mathbf{k}$ in the laser field, evaluated at the complex saddle point $t_s=t+i\tau$, which satisfies the standard saddle-point equation

$$\varepsilon_{\mathbf{k}}(t_s)+I_1=0.\tag{4}$$

In the tunneling regime specified by the condition $\gamma\ll1$, where $\gamma=\omega\sqrt{2I_1}/F_0$ is the Keldysh parameter [32], Eq. (4) can be approximately solved by keeping only the leading terms with respect to this small parameter, so that $\omega t=O(1)$ and $\omega\tau=O(\gamma)$. In this approximation, the imaginary part of Eq. (4) is

$$\mathbf{v}_{\mathbf{k}}(t)\cdot\mathbf{F}(t)\equiv\mathbf{v}_{\mathbf{k}\perp}\cdot\mathbf{F}(t)=0,\tag{5}$$

where $\mathbf{v}_{\mathbf{k}\perp}$ denotes the component of $\mathbf{v}_{\mathbf{k}}$ in the polarization plane. By putting $\cosh\omega\tau\approx1+(\omega\tau)^2/2$ and $\sinh\omega\tau\approx\omega\tau$ in the real part of Eq. (4), one easily finds the imaginary part of the saddle point

$$\omega\tau=\pm\sqrt{\frac{2[\varepsilon_{\mathbf{k}}(t)+I_1]\omega^2}{\ddot{\varepsilon}_{\mathbf{k}}(t)}}.\tag{6}$$

The real part t of the stationary point satisfies Eq. (5) and may be interpreted as the time of ionization. The equation itself means that at the exit of the tunnel the electron's velocity is perpendicular to the instantaneous field $\mathbf{F}(t)$. Equation (5) is equivalent to $\dot{\varepsilon}_{\mathbf{k}}(t)=0$ and says literally that the kinetic energy has an extremum at the time of ionization t. Since, by definition, τ is real, we must have

$$\ddot{\varepsilon}_{\mathbf{k}}(t)=\mathbf{F}^2(t)+\mathbf{v}(t)_{\perp}\cdot\dot{\mathbf{F}}(t)>0\tag{7}$$

in Eq. (6), so that the electron appears in the continuum with drift momentum $\mathbf{k}$ at the instant of time when its kinetic energy reaches a minimum. Together with the condition $\gamma\ll1$, Eq. (7) defines the applicability domain for the analytical expression (2). Since, for circular polarization, $\mathbf{v}(t)\cdot\dot{\mathbf{F}}(t)=-\mathbf{F}^2(t)$, expression (2) cannot be valid in this case. Indeed, already for $|\xi|$ close to unity, it is no longer valid. Substitution of the imaginary part (6) into the amplitude (3) and evaluation of $|M(\mathbf{k})|^2$ immediately give the exponent of the rate (2).

For the laser field propagating along the z axis, and with the unit vector $\mathbf{n}_{\perp}(t)$ in the polarization plane orthogonal to the field $\mathbf{F}(t)$, the solution of Eq. (5) is parametrized by

$$\mathbf{v}(t)=v_0\mathbf{n}_{\perp}(t)+v_z\mathbf{e}_z.\tag{8}$$

With this initial condition, the velocity in the laser field at times $\tilde{t}>t$ varies according to

$$\mathbf{v}(\tilde{t})=\mathbf{v}(t)-\mathbf{A}(\tilde{t})+\mathbf{A}(t).\tag{9}$$

Hence, an electron ionized at the time t possesses the drift momentum

$$\mathbf{k}=\mathbf{v}(t)+\mathbf{A}(t).\tag{10}$$

In standard saddle-point calculations, Eqs. (4) and (10) are used to find the parameters (t,v_0,v_z) as functions of the drift momentum $\mathbf{k}$ and, eventually, the transition rate $|M(\mathbf{k})|^2d^3k$ into the volume d^3k. For our model (1) we need, however, the rate as a function of the ionization time t. To this end, we consider (t,v_0,v_z) as new independent variables instead of (k_x,k_y,k_z). With account of the Jacobian

$$d^3k=[\ddot{\varepsilon}_{\mathbf{k}}(t)/F(t)]dtdv_0dv_z,\tag{11}$$

we arrive at the differential rate of ionization at time t with the transverse velocities v_0 and v_z. In addition, the rate so obtained is multiplied by the factor $[2F_a/F(t)]^2$, which is the Coulomb tunneling correction for subbarrier motion [34]. With this prefactor, after integration over the initial velocities, the rate (2) reproduces the total tunneling-ionization probability per unit time for the $1s$ state of a hydrogenlike atom in a quasistatic electric field $F(t)$ [35].

B. Condition of return

The time $t'(t)>t$ is determined by the condition that the electron liberated via tunneling at time t returns to its parent ion (at the origin) at t':

$$\int_t^{t'} d\tilde{t}\mathbf{v}(\tilde{t}) = 0. \tag{12}$$

In the z direction Eq. (12) requires that $v_z \equiv k_z = 0$. The remaining two components

$$[\xi\omega v_0/F(t) + 1](\omega t' - \omega t)\cos\omega t - (\sin\omega t' - \sin\omega t) = 0,$$

$$[\omega v_0/F(t) + \xi](\omega t' - \omega t)\sin\omega t + \xi(\cos\omega t' - \cos\omega t) = 0, \tag{13}$$

allow one to determine the return time t' and the initial velocity v_0 for a given start time t. Namely, the solution $t' = t'(t)$ has to be determined from

$$(1 - \xi^2)(\omega t' - \omega t)\cos\omega t \sin\omega t - \sin\omega t(\sin\omega t' - \sin\omega t) - \xi^2 \cos\omega t(\cos\omega t' - \cos\omega t) = 0, \tag{14}$$

and then

$$v_0 = -\frac{\xi F(t)}{\omega}\left(1 + \frac{\cos\omega t' - \cos\omega t}{(\omega t' - \omega t)\sin\omega t}\right). \tag{15}$$

The ionization time t enters the argument of the δ function in Eq. (1) via the photoelectron energy at the time of return

$$E(t') = \frac{1}{2}[\mathbf{v}(t) + \mathbf{A}(t) - \mathbf{A}(t')]^2. \tag{16}$$

Since Eqs. (13)–(15) are invariant under the translation $(\omega t, \omega t') \to (\omega t + \pi, \omega t' + \pi)$, it is sufficient to investigate the solutions and the respective orbits for $0 \le \omega t \le \pi$. It is worth noting that, even though v_0 does not change under the aforementioned translation, the respective vectors of the initial velocity have opposite directions due to the opposite directions of the unit vectors $\mathbf{n}_\perp(\omega t)$ and $\mathbf{n}_\perp(\omega t + \pi)$. For tunneling at the field phases ωt and $\omega t + \pi$, the respective phases upon the return differ by π, too. For this reason, the integrand in Eq. (1) does not change under the transformation $(\omega t, \mathbf{p}_1, \mathbf{p}_2) \to (\omega t + \pi, -\mathbf{p}_1, -\mathbf{p}_2)$ and, in consequence, the six-dimensional distribution possesses inversion symmetry so that $w(\mathbf{p}_1, \mathbf{p}_2) = w(-\mathbf{p}_1, -\mathbf{p}_2)$.

The ellipticity enters Eq. (14) to the order of ξ^2. Hence, as long as $\xi^2 \ll 1$, its solutions do not change very much compared with the case of linear polarization. In particular, returns are possible for start times t in the two quarters of the laser period that follow the field maxima, $\pi/2 \le \omega t \le \pi$ and $3\pi/2 \le \omega t \le 2\pi$ in our case. For some intervals of the start time t, there are several solutions $t_1' < t_2' < t_3' < \cdots$ for the return time t', which we will refer to as the first return, the second return, etc. (see Fig. 1). Upon each return at the time t_n' $(n = 1, 2, \ldots)$, impact ionization may occur, and the respective contributions are to be added in the yield (1). In order not to burden the notation, we will not write down this sum explicitly. Rather, we specify that in the rate (1), as well in the distributions below, the integral over the time t must be understood as

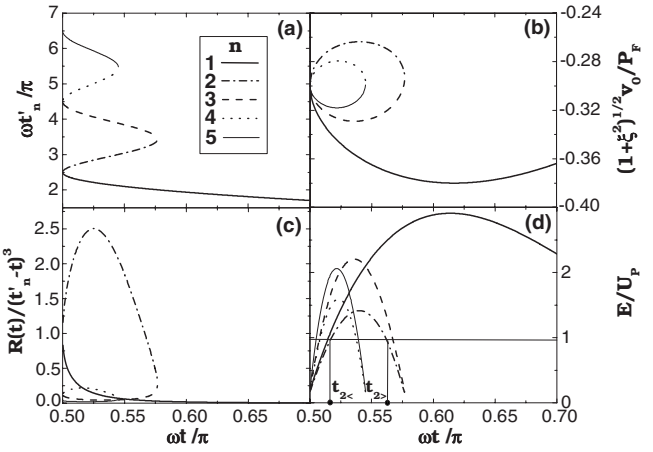

FIG. 1. (a) Dimensionless return time $\omega t_n'/\pi$, (b) initial transverse velocity scaled by the major axis of the polarization ellipse, $\sqrt{1+\xi^2}v_0/P_F$ with $P_F = F_0/\omega$, (c) the product of the tunneling rate and the spreading factor $(t_n' - t)^{-3}$ in arbitrary units, and (d) the electron kinetic energy upon its return in units of the ponderomotive energy $E(t)/U_P$ are shown as functions of the dimensionless ionization time $\omega t/\pi$. Results are only shown for $0.5\pi \le \omega t \le 0.7\pi$. For $0.5 \le \omega t/\pi \lesssim 0.575$ multiple returns exist. The plots include results for the first five returns $n = 1, \ldots, 5$ as specified in the inset of panel (a). The ellipticity is $\xi = 0.3$. In panel (d) the horizontal line shows the scaled second ionization potential I_2/U_P for NSDI of neon ($I_2 = 1.51$ a.u.) by a Ti:sapphire laser field ($\omega = 0.057$ a.u.) with intensity 8.0×10^{14} W/cm^2. Its intersections with the curves $E(t)/U_P$ determine the intervals $t_{n<} \le t \le t_{n>}$ of the ionization time for which impact ionization of the second electron is classically allowed. The values $t_{2<}$ and $t_{2>}$ are shown for the second return. We refer to the solutions denoted by no. 1 as the first return or the shortest orbit, to all others as "long orbits" [36].

$$\int dt\Phi(t,t') \Rightarrow \sum_n \int dt\Phi(t,t_n'). \tag{17}$$

We now turn to a key issue of this work: In order to be able to return to its parent ion the electron must tunnel out with the *nonzero* velocity $v_0\mathbf{n}_\perp(t)$ and, hence, have nonzero kinetic energy $\varepsilon_\mathbf{k}(t) = v_0^2/2$. (For linear polarization, $v_0 = 0$.) The price to be paid for the electron to return, compared with the case of linear polarization, is a lower value of the corresponding ionization rate due to the factor $[1 + v_0^2/(2I_1)]^{3/2} > 1$ in the exponential of the rate (2). The example shown in Fig. 1(c) demonstrates a remarkable peculiarity of the case of elliptical polarization: The contribution $R(t)/(t' - t)^3$ to the distribution (1) corresponding to the second return $(t' \equiv t_2')$ is larger than the one for the first return $(t' \equiv t_1')$. The reason is related to the presence of the initial velocity in the rate (2). The minimum of $|v_0|$ for $n = 2$ [cf. Fig. 1(b)] causes the maximum of the respective curve in Fig. 1(c). The nonmonotonic dependence of v_0 on the start time stems from the second term in brackets in Eq. (15), which is small due to the large value of the travel time in the denominator.

There is another difference compared with the case of linear polarization: For the latter, the *same* trajectory after its first return may return again and again. For elliptical polar-

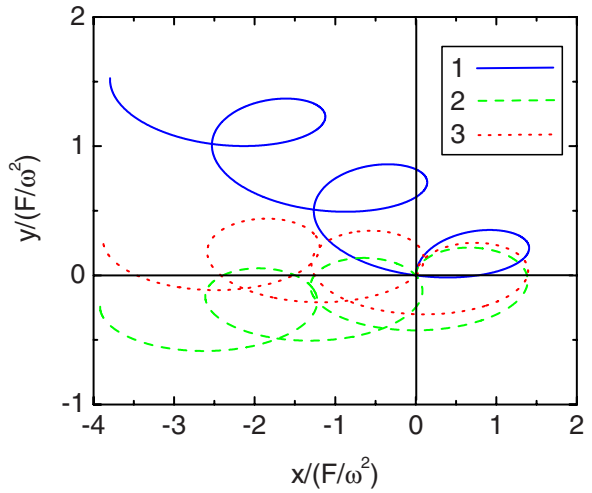

FIG. 2. (Color online) Three returning trajectories for the ellipticity $\xi=0.3$, which all start at $\omega t=1.80$ at the origin but with different initial velocities v_0, which are reflected in the different gradients at the start time $\omega t=1.80$. When orbit no. 1 returns to the origin, this is the first time it intersects the line $x=0$. For orbit no. 2, it is the second time, for orbit no. 3 the third, and so on. For linear polarization, the initial velocity v_0 is zero, and all orbits are identical.

ization, this is not so because each return is enforced by having a specific value of the initial velocity v_0, which is different for different returns; cf. Fig. 2 for an example [36].

III. PARTLY INTEGRATED DISTRIBUTIONS

Experiments do not normally measure the sixfold differential rate (1), but integrate over some of the momentum components. For the rate (1) with constant form factor, this can easily be done analytically as described for linear polarization in Ref. [24]. The same technique can be used for elliptical polarization. Namely, the δ function is replaced by its Fourier representation

$$\delta(x) = \frac{1}{2\pi}\int_{-\infty}^{\infty} d\lambda\, \exp(-i\lambda x). \tag{18}$$

The integrations over the components of the momenta $\mathbf{p}_1$ and $\mathbf{p}_2$ are now independent and can be carried out analytically. The remaining integration over λ is done with the help of the integral [37]

$$\int_{-\infty}^{\infty} \frac{d\lambda}{(i\lambda+\epsilon)^{\nu}}\exp(i\lambda B) = \frac{2\pi}{\Gamma(\nu)}B_+^{\nu-1}, \tag{19}$$

where $B_+^{\nu}=B^{\nu}\theta(B)$, with $\theta(B)$ the Heaviside step function and $\epsilon\to+0$. The factor $B_+^{\nu-1}$ reflects the momentum-space volume available for the motion with the configuration of momenta under consideration. The function B is given by the argument of the δ function in the fully differential rate (1) with those terms dropped that are related to the momentum components that have been integrated over. Each integration with infinite limits over a momentum component adds 1/2 to the value of the parameter ν. Therefore, the integer or half-integer value of ν depends on the number of integrations that have been carried out. Distributions resulting from integrations over different sets of momentum projections will be distinguished by their arguments, which show those variables that were not integrated out. We will evaluate distributions of the momentum components in the polarization plane. Hence, in all cases considered below the differential rate (1) is integrated over the projections along the direction of propagation, $-\infty<p_{1z},p_{2z}<\infty$.

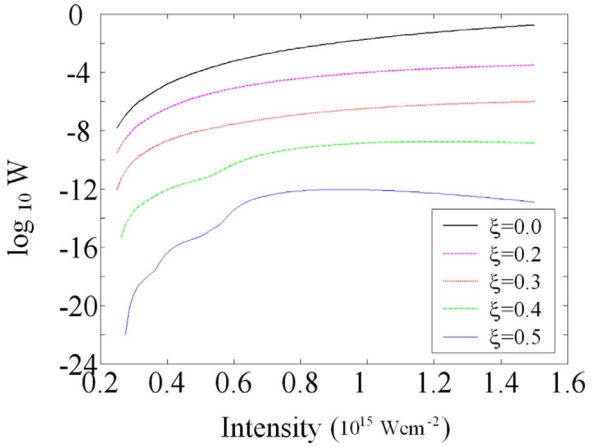

FIG. 3. (Color online) Total yield of doubly charged ions calculated from Eqs. (20) and (21) for neon as a function of intensity at different ellipticities.

A. Total yield

The total yield of doubly charged ions is obtained by integration over all momentum components of both electrons ($\nu=3$) as follows:

$$w \equiv \int d^3\mathbf{p}_1 d^3\mathbf{p}_2 w(\mathbf{p}_1,\mathbf{p}_2) \sim \int dt \frac{R(t)}{(t'-t)^3}B_+^2, \tag{20}$$

with

$$B = E(t') - I_2. \tag{21}$$

The condition $E(t_n')\geq I_2$ defines (modulo T) the actual range of integration $t_{n<}\leq t\leq t_{n>}$ for the respective term in the sum over n in the rate (20) [see Eq. (17)]. Figure 1(d) shows that, for given ionization potential, the left and right thresholds $t_{n<}$ and $t_{n>}$ for a particular return $n\geq 2$ approach each other more and more closely with increasing return number. Within these narrow intervals, the electric field and thus the factor $2F_a/(3\sqrt{\ddot{\varepsilon}_{\mathbf{k}}(t)})$ in the exponent of the rate (2) do not vary appreciably so that the behavior of the rate is determined mainly by the nonmonotonic dependence of the initial velocity on the start time [cf. Fig. 1(b)]. Results are shown in Fig. 3. For fixed intensity, the yield of doubly charged ions rapidly decreases with increasing ellipticity. With increasing intensity (assuming ellipticity and all other parameters fixed), it monotonically increases so long as $\xi\lesssim 0.4$. Around this ellipticity, the behavior of the curves changes. At $\xi=0.5$, there appears a flat maximum at some intensity and thereafter the yield decreases. For the larger ellipticities

$\xi=0.4$ and $\xi=0.5$, the slope of the total yield in Fig. 3 displays pronounced variations. These occur whenever the leading role in the sum over n is taken over by a new term.

B. Ion-momentum distributions

Experiments often present distributions of the total electron momentum $\mathbf{P}=(\mathbf{p}_1+\mathbf{p}_2)/\sqrt{2}$, while the relative momentum $\mathbf{p}=(\mathbf{p}_1-\mathbf{p}_2)/\sqrt{2}$ is integrated over. Since the momentum of the laser photons is negligibly small, momentum conservation implies that the ion momentum is equal to $-\sqrt{2}\mathbf{P}$. Analysis of the two-dimensional ion-momentum distribution in the polarization plane provides a qualitative understanding of the effects caused by a nonzero ellipticity. This distribution $w(P_x,P_y)$, where the components P_z and p_x,p_y,p_z have been integrated out, is given by

$$w(P_x,P_y) \equiv \int dP_z d^3\mathbf{p} w(\mathbf{p}_1,\mathbf{p}_2) \sim \int dt \frac{R(t)}{(t'-t)^3} B_+(P_x,P_y). \tag{22}$$

For this case, $\nu=2$ and

$$B(P_x,P_y) = E(t') - I_2 - \frac{[P_x-\sqrt{2}A_x(t')]^2}{2} - \frac{[P_y-\sqrt{2}A_y(t')]^2}{2}. \tag{23}$$

For fixed momenta P_x and P_y, the condition $B(P_x,P_y)\geq 0$ determines the limits of integration over time for each term in the sum over n in Eq. (22). On the other hand, for fixed time t, the same condition determines the classically allowed region of momentum space. The density plots in Fig. 4, which are evaluated from Eq. (22), reveal some basic effects specific to an elliptically polarized field. The two-dimensional (2D) ion-momentum distribution consists of two parts, which are practically disconnected and centered near the major axis of the polarization ellipse. Inspection of the two upper rows shows that, starting from linear polarization an increase of ellipticity results in (i) a very pronounced drop of the yield as demonstrated by the numbers in the lower right corner of each panel and (ii) an obvious reduction of the width of the distribution. Yet another effect, which becomes evident for ellipticities around $\xi\approx 0.4$, is a slight rotation of the 2D ion-momentum distribution in the direction opposite to the rotation of the laser field.

The most important message of Fig. 4 becomes clear when we compare the second and the third row. In contrast to the distributions displayed in the second row, those in the third are based on the contribution of only the first return. The latter are much smaller in magnitude, but extend over a relatively larger range of momenta, and the above-mentioned rotation is in the opposite direction, in the same direction as the laser field rotates. Table I presents more detailed quantitative information on the contributions from the various returns. In a linearly polarized field, the contributions of the late returns monotonically decrease with increasing t' due to the quantum spreading $(t'-t)^{-3}$ and a smaller value of $[E(t)]_{\max}$ [see Fig. 1(d)], which results in a reduction of the available phase space. In the case of elliptical polarization, in addition to these factors the contribution of a given return

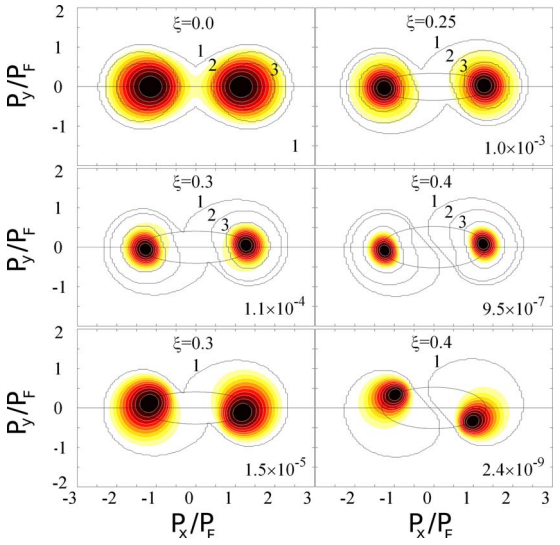

FIG. 4. (Color online) The 2D ion-momentum distribution for ionization of neon by the field of a Ti:sapphire laser with intensity 8×10^{14} W/cm^2 for different ellipticities. In the upper two rows, the contributions from the first six returns were summed while the third row presents the contribution from the first return only. The numbers in the lower right corner of each panel specify the relative height of the maxima with respect to linear polarization. In each panel, a thin solid line presents a parametric plot of the vector potential for the respective ellipticity. Additional thin solid lines exhibit the boundaries of the classically allowed regions for those returns whose numbers n are given next to the respective curves.

depends on the initial velocity v_0. Since this enters the tunneling rate (2) exponentially, even a small variation with ellipticity can have a large effect on the magnitude of the contribution. In particular, for $\xi=0.3$, the minimum of v_0 for the second return [see Figs. 1(b) and 1(c)] increases the tunneling rate to an extent that it overcomes the quantum spreading. The net result is that the contribution of the second return becomes dominant.

The momentum distribution (22) is a superposition of contributions with different widths. The width of any partial contribution generated by a late return is less than the width of the first return. When with increasing ellipticity the leading role in the sum goes from the first to the second return, the resulting distribution narrows. Similarly, with increasing ellipticity, the maxima of the partial contributions with $n\geq 2$ remain near the major axis, whereas the contribution of the first return rotates and shifts away from it (see the third row in Fig. 4). Since an increase of ξ boosts the contributions of the late returns, the resulting total distribution assumes its maximum near the major axis as can be seen from the second row in Fig. 4.

At low intensity, when $[E(t)]_{\max}<I_2$, the return number n does not contribute to the distribution (1). For this reason, for Ne at the intensity 4×10^{14} W/cm^2 and ellipticities from zero up to about $\xi=0.4$ there are no contributions from the second return. Contributions from $n=4,6$ are negligibly small when $\xi\to 0$ and strictly absent for larger ellipticities. Under these conditions, Table II shows that the contribution from the first return is the largest for ellipticities $\xi\leq 0.4$. Nevertheless, the ion-momentum distribution does not ex-

TABLE I. Relative values of the maxima of the momentum distributions evaluated separately for the returns $n=1$ to $n=6$ at the intensity 8.0×10^{14} W/cm^2. The bottom row gives for each value of ξ the ratio of the maxima for elliptical polarization and for linear polarization.

n	$\xi=0.0$	$\xi=0.25$	$\xi=0.30$	$\xi=0.35$	$\xi=0.40$
1	1.000	1.000	0.180	0.020	0.018
2	0.015	0.780	1.000	1.000	1.000
3	0.014	0.130	0.066	0.020	0.0047
4	0.002	0.070	0.078	0.062	0.047
5	0.0019	0.024	0.015	0.006	0.0019
6	0.0005	0.016	0.016	0.0012	0.0079
	1.0	4.4×10^{-4}	6.0×10^{-5}	7.2×10^{-6}	5.6×10^{-7}

hibit a noticeable rotation, which according to the third row of Fig. 4 we might have expected from the contribution of the first return. The reason is that this rotation is rather weak at low intensity and becomes evident only around an ellipticity of $\xi\approx0.4$. But at such a large ellipticity the contribution of the third return, which is centered near the major axis, has a comparable value so that the resulting total distribution maximizes closer to the major axis.

Ion-momentum distributions along the major axis of the laser polarization ellipse can be deduced similarly to Eq. (22) by doing the additional integration over P_y. In this case, $\nu=2.5$ and

$$w(P_x)\sim\int dt\frac{R(t)}{(t'-t)^3}B_+^{3/2}(P_x), \tag{24}$$

where

$$B(P_x)=E(t')-I_2-\frac{[P_x-\sqrt{2}A_x(t')]^2}{2}. \tag{25}$$

The distribution along the minor axis is obtained from Eqs. (24) and (25) by the substitution $x\rightarrow y$. Results of a numerical evaluation are shown in Fig. 5.

Starting from linear polarization, both the double-humped distribution of P_x in Fig. 5(a) and the smooth bell-shaped P_y distribution in Fig. 5(b) preserve their shape with increasing ellipticity, though all peaks narrow. Such a behavior is in complete agreement with the properties of the 2D distribution discussed above. If only the first return is accounted for, the longitudinal distribution [Fig. 5(c)] is not qualitatively different from the previous result where six returns are included. In contrast, for the large ellipticity $\xi=0.5$, the transverse distribution [Fig 5(b)] is bell shaped when the first six returns are included while double humped for the first return only [Fig. 5(d)]. This is a different manifestation of the same effect that we discussed in Fig. 4 for $\xi=0.4$. Recall that the rotation of the distribution in the (P_x,P_y) plane is only significant for the first return. If the 2D distributions of Fig. 4 are projected on the y axis, the results of Figs. 5(b) and 5(d) are obtained.

C. Electron–electron correlation

The distribution $w(p_{1x},p_{2x})$ obtained when the other momentum components have been completely integrated over (from minus infinity to infinity) consists of two symmetric spots on the main diagonal $p_{1x}=p_{2x}$ and behaves with increasing ellipticity similarly to the 2D ion-momentum distribution. Its shape remains qualitatively the same as in the case of linear polarization but the yield rapidly drops and the width of the maxima on the main diagonal decreases. A more interesting shape of the (p_{1x},p_{2x}) correlation can be observed when the other momentum components are not completely integrated but only restricted to some intervals. Let us consider the distribution of the momentum projections p_{1x} and

TABLE II. The same as Table I but at the intensity 4.0×10^{14} W/cm^2. A dash means that the respective return does not contribute at all.

n	$\xi=0.0$	$\xi=0.25$	$\xi=0.30$	$\xi=0.40$	$\xi=0.50$
1	1.000	1.000	1.000	1.000	0.150
2	—	—	—	—	—
3	0.010	0.044	0.092	0.643	1.000
4	1.98×10^{-5}	—	—	—	—
5	0.011	0.0057	0.013	0.110	0.180
6	4.39×10^{-5}	—	—	—	—
	1.0	2.8×10^{-3}	1.7×10^{-4}	8.2×10^{-8}	2.4×10^{-10}

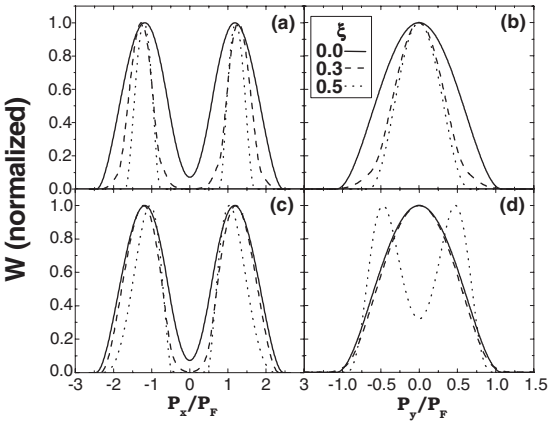

FIG. 5. Ion-momentum distributions along the major axis [(a) and (c)] and the minor axis [(b) and (d)] of the laser polarization ellipse for different ellipticities [explained in the inset of (b)] for the parameters of Fig. 4. The contributions of the first six returns are accounted for in (a) and (b), while (c) and (d) show the corresponding distributions with only the first return included. The curves are normalized to unity at their maxima. The momenta are scaled by $P_F=F_0/\omega$.

p_{2x} (parallel to the major axis), which comes about by integration of the distribution (1) over all values of p_{1z} and p_{2z} while the components p_{1y} and p_{2y} (parallel to the minor axis) are fixed to the values $(\tilde{p}_{1y},\tilde{p}_{2y})$:

$$w(p_{1x},p_{2x}|\tilde{p}_{1y},\tilde{p}_{2y}) \sim \int dt \frac{R(t)}{(t'-t)^3}\theta(B), \tag{26}$$

$$B \equiv B(p_{1x},p_{2x}|\tilde{p}_{1y},\tilde{p}_{2y}) = \left\{E(t) - I_2 - \frac{[\tilde{p}_{1y}-A_y(t')]^2}{2} - \frac{[\tilde{p}_{2y}-A_y(t')]^2}{2}\right\} - \frac{[p_{1x}-A_x(t')]^2}{2} - \frac{[p_{2x}-A_x(t')]^2}{2}. \tag{27}$$

The term in curly brackets is the energy available for both electrons for their motion in the x direction. With fixed $\tilde{p}_{1y}$ and $\tilde{p}_{2y}$ it is, in general, different for opposite directions of the laser field. This is definitely so if $\tilde{p}_{1y}$ and $\tilde{p}_{2y}$ have the same sign. The exception is the case of $\tilde{p}_{1y}=-\tilde{p}_{2y}$, when the available energy remains the same from one laser half-period to the next. The two peaks of the (p_{1x},p_{2x}) distribution are produced in two adjacent half-periods with opposite directions of the field. Unequal available energies lead to asymmetric volumes of the classically allowed momentum space and, in consequence, to asymmetric peaks of the distribution. Technically, contributions from two half-periods are different because of different integration limits over time in the rate (26), which are determined by the condition $B \geq 0$. Which one of the two contributions (for a given return) will be larger depends on the length and on the position of the integration interval with respect to the maximum of the tunneling-return rate shown in Fig. 1(c).

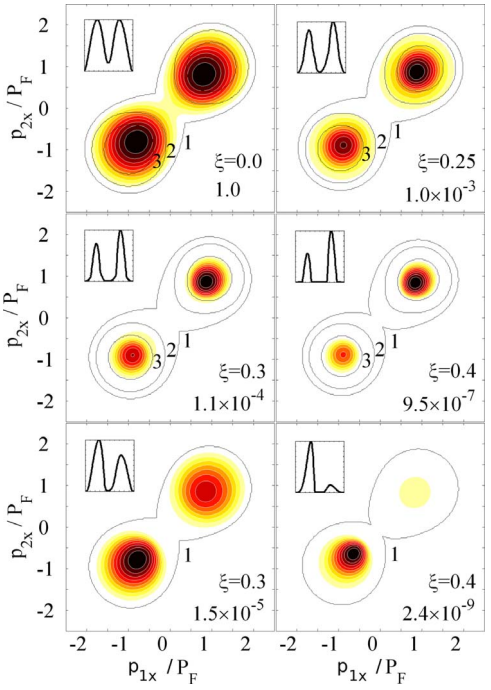

FIG. 6. (Color online) The distribution $w(p_{1x},p_{2x}|p_{1y}>0,p_{2y}>0)$ for various ellipticities evaluated with account of six returns (two upper rows). The third row presents the contribution from the first return only. The numbers in the lower right corners give the relative suppression of the larger maximum in the panel with respect to linear polarization. The boundaries of the classically allowed regions for several specified returns are exhibited and identified by the numbers n next to the respective curve. The insets in the upper left corners show the cuts through the corresponding 2D distributions along the $p_{1x}=p_{2x}$ diagonal. The parameters are those of Fig. 4.

Measuring the fourfold differential distribution (26) is a daunting task. However, the asymmetry persists if we integrate the distribution over all positive values of $\tilde{p}_{1y}$ and $\tilde{p}_{2y}$. The corresponding distributions $w(p_{1x},p_{2x}|\tilde{p}_{1y}>0,\tilde{p}_{2y}>0)$ are plotted in Figs. 6 and 7 for two different intensities. The ratios between the contributions of the various returns are practically the same as they were for the ion-momentum distribution at the respective intensities in Tables I and II. Comparison of the results shown in the second and third rows of Fig. 6 once again makes evident the necessity to consider the contributions of the late returns: If the first six returns are included, the e-e correlation assumes its absolute maximum in the first quadrant; if only the first return is considered (the last row of Fig. 6), the absolute maximum is found in the third quadrant. Hence, the location of the absolute maximum constitutes a very distinct criterion for the significance of the longer orbits. The detailed behavior of the e-e correlation is quite involved and not accessible to simple qualitative explanations. For example, at the higher intensity of 8×10^{14} W/cm^2, the larger of the two maxima remains located in the first quadrant of the (p_{1x},p_{2x}) plane when the ellipticity increases. In contrast, at the lower intensity of 4×10^{14} W/cm^2, it oscillates between the first and third quadrants.

The distributions in Figs. 6 and 7 are conveniently characterized by the asymmetry parameter

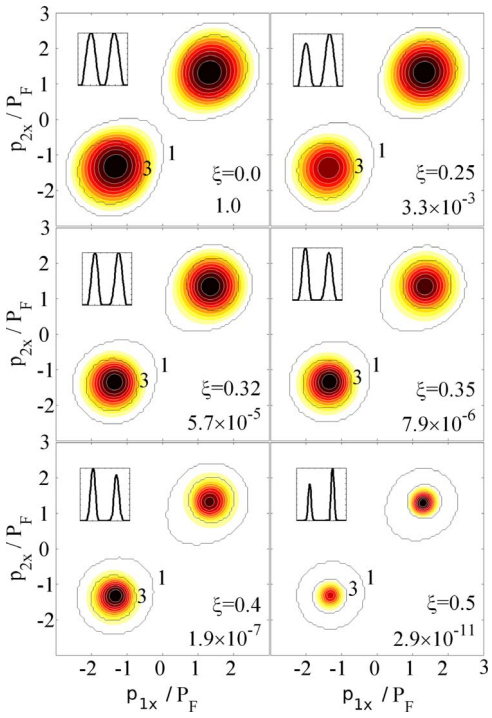

FIG. 7. (Color online) The same as Fig. 6 except that the intensity is 4.0×10^{14} W/cm^2 and the contributions from the first six returns are accounted for in all panels.

$$\alpha = (w_1 - w_3)/(w_1 + w_3), \tag{28}$$

where w_1 and w_3 are the integrated populations of the first and the third quadrant, respectively. Figure 8 shows that the dependence of the asymmetry on the ellipticity ξ is not monotonic for larger ξ. Local maxima and minima develop. This tendency is more pronounced for the lower intensity, where the asymmetry twice changes its sign so that the total maximum of the electron-electron correlation moves from the first to the third quadrant and back again. A closer analysis shows that, for even returns, the stronger maximum remains for all ellipticities in the same quadrant, whereas it can change quadrants at some ellipticity for the odd returns. That, in combination with the relative magnitude of the contributions from different returns, explains the evolution with ellipticity of the asymmetry α as well as of the density plots.

Specifically, at the higher intensity of 8×10^{14} W/cm^2, when ξ departs from zero the first return dominates the sum (26) and its contribution is maximal in the first quadrant. The decrease of α after ξ=0.18 indicates that this contribution is about to move from the first into the third quadrant. But somewhere around $\xi\approx0.2$ the leading role in the sum (26) goes to the contribution from the second return, and the latter is maximal in the first quadrant, like the first return was for small ξ. As a result, the total distribution summed over all returns retains its largest maximum in the first quadrant for all ellipticities. At the lower intensity of 4×10^{14} W/cm^2, the contribution of the second return is absent (cf. Table II) and the first return dominates in a wider range of ellipticities up to $\xi\approx0.4$. In this range, α keeps decreasing after the local maximum until it changes its sign so that the largest maximum of the distribution moves to the third quadrant. For ξ further increasing, α stays negative until the sum of the contributions of the third and fifth return exceeds the contribution of the first and the resulting distribution returns to the first quadrant.

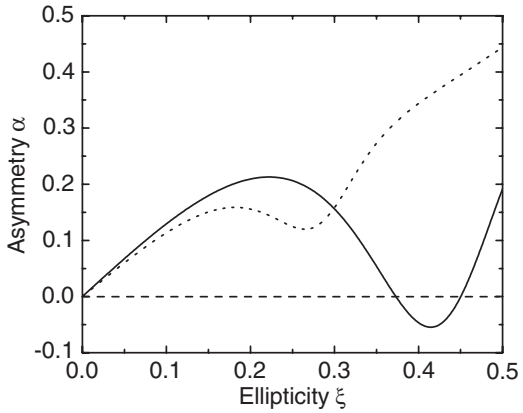

FIG. 8. Asymmetry (28) as a function of ellipticity at intensities 8.0×10^{14} W/cm^2 (dotted line) and 4.0×10^{14} W/cm^2 (solid line). At the higher intensity, a local maximum and minimum are at ξ =0.18 and ξ=0.27, respectively. At the lower intensity, the maximum and minimum are at ξ=0.22 and ξ=0.42, respectively, and the asymmetry vanishes at ξ=0.37 and ξ=0.45.

An asymmetry of the populations in the first and third quadrants of about ten percent is already present at an ellipticity of $\xi\approx0.1$. At this ellipticity, the total yield has decreased by no more than a factor of 3 with respect to linear polarization. This should leave the observation of the asymmetry within reach of the present state of the art.

IV. CONCLUSIONS

In conclusion, on the basis of a semiclassical model that treats the electron-electron interaction as a three-body contact interaction, we have investigated various differential distributions of the ion and electron momenta in nonsequential double ionization by an elliptically polarized laser field. The main result of our study is that for sufficiently large ellipticity the main contribution to the rate (1) no longer comes from the first return of the photoelectron to its parent ion, as is typical for linear polarization, but from longer orbits. The second through fourth orbits, for which the travel time is in between one and three laser periods, contribute mostly for $\xi\simeq0.3-0.4$ and intensities $\simeq10^{15}$ W/cm^2. As a result, the shape of the partly integrated distributions qualitatively depends upon how many orbits contribute, i.e., on the duration of the laser pulse. Going from pulses that are long enough to sustain several returns to very short pulses where only the trajectories corresponding to the first return contribute, one should observe qualitative effects, such as the formation of a dip in the transverse ion momentum distribution (cf. Fig. 5) or the maximum in the partially integrated electron-electron correlation moving from the first quadrant to the third (cf.

Fig. 6). The observation of such effects will provide a direct justification for the quantum orbit picture, in general, and for the significance of long orbits, in particular. With currently available ultrashort infrared pulses [38] such measurements should be possible. Note, however, that in view of the low count rate, which quickly decreases with increasing ellipticity, an experimental realization requires a laser with very high repetition rate, such as it was used in Refs. [10,12].

ACKNOWLEDGMENTS

We are grateful to H. Rottke and D. F. Zaretsky for valuable discussions. This work was supported by Deutsche Forschungsgemeinschaft (Project No. 436 RUS 113/832/0-1), the Russian Foundation for Basic Researches (Grants No. 05-02-04016 and No. 06-02-16916), and the NSERC Special Opportunity Program, Canada.

[1] M. Lewenstein, Ph. Balcou, M. Yu. Ivanov, A. L'Huillier, and P. B. Corkum, Phys. Rev. A **49**, 2117 (1994).

[2] P. Salières *et al.*, Science **292**, 902 (2001).

[3] P. Agostini and L. F. DiMauro, Rep. Prog. Phys. **67**, 813 (2004).

[4] W. Becker, F. Grasbon, R. Kopold, D. B. Milošević, G. G. Paulus, and H. Walther, Adv. At., Mol., Opt. Phys. **48**, 35 (2002).

[5] D. B. Milošević, E. Hasović, M. Busuladžić, A. Gazibegović-Busuladžić, and W. Becker, Phys. Rev. A **76**, 053410 (2007).

[6] E. S. Toma, Ph. Antoine, A. de Bohan, and H. G. Muller, J. Phys. B **32**, 5843 (1999).

[7] S. V. Popruzhenko, Ph. A. Korneev, S. P. Goreslavski, and W. Becker, Phys. Rev. Lett. **89**, 023001 (2002).

[8] A. M. Perelomov, V. S. Popov, and M. V. Terent'ev, Zh. Eksp. Teor. Fiz. **51**, 309 (1966) [Sov. Phys. JETP **24**, 207 (1966)].

[9] S. P. Goreslavskii and S. V. Popruzhenko, Zh. Eksp. Teor. Fiz. **110**, 1200 (1996) [JETP **83**, 661 (1996)].

[10] G. G. Paulus, F. Zacher, H. Walther, A. Lohr, W. Becker, and M. Kleber, Phys. Rev. Lett. **80**, 484 (1998).

[11] M. Bashkansky, P. H. Bucksbaum, and D. W. Schumacher, Phys. Rev. Lett. **60**, 2458 (1988).

[12] G. G. Paulus, F. Grasbon, A. Dreischuh, H. Walther, R. Kopold, and W. Becker, Phys. Rev. Lett. **84**, 3791 (2000).

[13] S. P. Goreslavski, G. G. Paulus, S. V. Popruzhenko, and N. I. Shvetsov-Shilovski, Phys. Rev. Lett. **93**, 233002 (2004).

[14] R. Kopold, D. B. Milošević, and W. Becker, Phys. Rev. Lett. **84**, 3831 (2000).

[15] V. V. Suran and I. P. Zapesochny, Sov. Tech. Phys. Lett. **1**, 420 (1975).

[16] A. l'Huillier, L. A. Lompré, G. Mainfray, and C. Manus, Phys. Rev. A **27**, 2503 (1983).

[17] P. B. Corkum, Phys. Rev. Lett. **71**, 1994 (1993).

[18] R. Dörner, Th. Weber, M. Weckenbrock, A. Staudte, M. Hattas, H. Schmidt-Böcking, R. Moshammer, and J. Ullrich, Adv. At., Mol., Opt. Phys. **48**, 1 (2002); A. Becker, R. Dörner, and R. Moshammer, J. Phys. B **38**, S753 (2005).

[19] C. Ruiz, L. Plaja, L. Roso, and A. Becker, Phys. Rev. Lett. **96**, 053001 (2006).

[20] A. Becker and F. H. M. Faisal, J. Phys. B **29**, L197 (1996).

[21] M. Yu. Kuchiev, J. Phys. B **28**, 5093 (1995).

[22] L.-B. Fu, J. Liu, and S.-G. Chen, Phys. Rev. A **65**, 021406(R) (2002); J. Chen and C. H. Nam, *ibid.* **66**, 053415 (2002).

[23] R. Panfili, S. L. Haan, and J. H. Eberly, Phys. Rev. Lett. **89**, 113001 (2002); P. J. Ho, R. Panfili, S. L. Haan, and J. H. Eberly, *ibid.* **94**, 093002 (2005).

[24] C. Figueira de Morisson Faria, H. Schomerus, X. Liu, and W. Becker, Phys. Rev. A **69**, 043405 (2004).

[25] C. Figueira de Morisson Faria, X. Liu, and W. Becker, *Progress in Ultrafast Intense Laser Science II* (Springer, Heidelberg, 2007), p. 65.

[26] D. N. Fittinghoff, P. R. Bolton, B. Chang, and K. C. Kulander, Phys. Rev. A **49**, 2174 (1994).

[27] P. Dietrich, N. H. Burnett, M. Yu. Ivanov, and P. B. Corkum, Phys. Rev. A **50**, R3585 (1994).

[28] G. D. Gillen, M. A. Walker, and L. D. Van Woerkom, Phys. Rev. A **64**, 043413 (2001).

[29] C. Guo, J. Phys. B **38**, L323 (2005).

[30] S. P. Goreslavskii, S. V. Popruzhenko, R. Kopold, and W. Becker, Phys. Rev. A **64**, 053402 (2001).

[31] A. Staudte *et al.*, Phys. Rev. Lett. **99**, 263002 (2007); A. Rudenko, V. L. B. de Jesus, T. Ergler, K. Zrost, B. Feuerstein, C. D. Schroter, R. Moshammer, and J. Ullrich, *ibid.* **99**, 263003 (2007).

[32] L. V. Keldysh, Zh. Eksp. Teor. Fiz. **47**, 1945 (1964) [Sov. Phys. JETP **20**, 1307 (1965)].

[33] F. H. M. Faisal, J. Phys. B **6**, L89 (1973); H. R. Reiss, Phys. Rev. A **22**, 1786 (1980).

[34] A. M. Perelomov and V. S. Popov, Zh. Eksp. Teor. Fiz. **52**, 514 (1967) [Sov. Phys. JETP **25**, 336 (1967)].

[35] L. D. Landau and E. M. Lifshitz, *Quantum Mechanics (Non-relativistic Theory)* (Pergamon Press, Oxford, 1977).

[36] To avoid confusion, we emphasize that our current nomenclature of "long orbits" deviates from that commonly used in the literature; cf., e.g., Refs. [4,7]. Normally, the electron momentum at the detector is held fixed and the solutions of the saddle-point equations are (t_k', t_k) $(k=1,2,\ldots)$, which can be ordered by their travel time $\tau_k \equiv t_k' - t_k$ so that $\tau_k > \tau_{k-1}$. The solution $(k=1)$ with the shortest travel time is called "the short orbit," the one with $k=2$ is called "the long orbit," and all others $(k>3)$ are "longer orbits." In this paper, we keep the ionization time t constant and consider the various return times $t_n'(t)$, which all require different initial velocities v_{0n} (and lead to different final momenta). Depending on the value of t, there may be just one or several solutions t_n' [cf. Fig. 1(a)]. We refer to the branch of solutions with the shortest travel times τ as the short orbits; viz., the solid line in Fig. 1(a). All others we refer to as longer orbits. Comparing nomenclatures, both the standard short orbit and long orbit of HHG just below the cutoff energy are short orbits in the sense of this paper, since they both lie on branch no. 1 in Fig. 1(a).

[37] I. S. Gradshteyn and I. M. Ryzhik, *Table of Integrals, Series, and Products* (Academic Press, New York, 1980).

[38] D. B. Milošević, G. G. Paulus, D. Bauer, and W. Becker, J. Phys. B **39**, R203 (2006).